Check for updates

Angewandte Chemie International Edition

Angewandte International Edition Chemie

GDCh German Chemical Society

How to cite: *Angew. Chem. Int. Ed.* **2026**, 65, e25822
doi.org/10.1002/anie.202525822

RESEARCH ARTICLE Hot Paper

Temperature-Potential Coupled Regulation of $LiPF_6$ Decomposition to Construct LiF Grain Boundary-Rich Interphase on Graphite Anode for Fast-Charging Li-Ion Batteries

Zhiyong Wang[1,2] | Wei Hao[1,2,3] | Tong Duan[1,4] | Shuang Wei[1,4] | Yuanmao Chen[1,2] | Tinghu Liu[5] | Jijiang Liu[1,2] | Yeliang Sheng[1,2] | Xinyang Yue[1,2] | Zulipiya Shadike[5] | Zheng Liang[1,2]

[1]Frontiers Science Center for Transformative Molecules, School of Chemistry and Chemical Engineering, Shanghai Jiao Tong University, Shanghai, China | [2]Zhangjiang Institute for Advanced Study, Shanghai Jiao Tong University, Shanghai, China | [3]School of Electrical Engineering, Shanghai Jiao Tong University, Shanghai, China | [4]Shanghai TANSUO Testing and Inspection Company, Shanghai, China | [5]Institute of Fuel Cells, School of Mechanical Engineering, Shanghai Jiao Tong University, Shanghai, China

Correspondence: Xinyang Yue (xinyangyue@sjtu.edu.cn) | Zulipiya Shadike (zshadike@sjtu.edu.cn) | Zheng Liang (liangzheng06@sjtu.edu.cn)

Received: 22 November 2025 | **Revised:** 8 January 2026 | **Accepted:** 20 January 2026

Keywords: fast charging | graphite anode | lithium-ion batteries | LiF grain boundary-rich SEI | $LiPF_6$ decomposition

ABSTRACT

Regulating the electrolyte decomposition to evolve a LiF-rich solid-electrolyte interphase (SEI) can reduce the energy barrier of the interfacial Li-ion transport toward fast-charging lithium-ion batteries. Due to the sluggish decomposition kinetics, $LiPF_6$, as a widely used Li salt in commercial cells, is unable to build a LiF-rich SEI. Therefore, expensive fluorinated electrolyte additives are needed. Herein, to eliminate the use of extra fluorinated species, based on the subtle electrochemical decomposition of $LiPF_6$ occurring ~2.28 V vs. Li^+/Li at 80°C, we developed a temperature-potential coupled formation (TPCF) protocol, which incorporates a constant-voltage step (2.28 V) at 80°C to stimulate $LiPF_6$ decomposition deeply, thereby generating a high-quality SEI uniformly covering the graphite particle surfaces. This TPCF-derived SEI is thin and dense, full of LiF grain boundaries, which could reduce the energy barriers of Li^+ desolvation and interfacial Li^+ diffusion. Simultaneously, this SEI exhibits a higher work function, effectively suppressing electron leakage to reduce the degeneration of the electrolyte and interphase. Consequently, after a simple TPCF process, the assembled graphite||$LiFePO_4$ full cell achieves stable cycling at a 6C rate, retaining 80% of its capacity after 3304 cycles and 70.5% after 8940 cycles, outperforming the counterparts.

1 | Introduction

The widespread adoption of electric vehicles, which primarily rely on lithium-ion batteries (LIBs), remains constrained by limited driving range and prolonged charging times [1]. The development of fast-charging technology is expected to alleviate the pervasive issue of "range anxiety" [2]. The United States Advanced Battery Consortium has set a target for extremely fast charging at a 4C charging rate, enabling batteries to reach 80% state of charge (SOC) within just 15 min [3]. However, high-rate charging induces significant electrochemical polarization within the battery, exacerbating Li plating on the graphite anode

Zhiyong Wang, Wei Hao, and Tong Duan contributed equally to this work.

Dedicated to the fifth anniversary of the Frontiers Science Center for Transformative Molecules

© 2026 Wiley-VCH GmbH

surface and substantially shortening cycle life [4]. The rate-determining step for fast-charging kinetics lies in the desolvation and subsequent transport of solvated lithium ions (Li^+) across the solid-electrolyte interphase (SEI) on the graphite particles [5].

An ideal SEI must exhibit high ionic conductivity to ensure Li^+ transport and excellent electronic insulation to block electron leakage for suppressing continuous electrolyte decomposition and SEI growth [6, 7]. Consequently, constructing the SEI with a dense inner inorganic layer, particularly LiF-rich, is an essential research focus of fast-charging batteries [8–10]. Various strategies have been proposed, including regulating the electrolyte solvation structure [11–13], designing novel electrolyte additives [14, 15], and constructing artificial SEI layers [16–18]. However, most approaches, such as localized high-concentrated electrolytes and fluorinated additives [14, 19–21], face obstacles for large-scale industrial application due to high costs and poor compatibility with conventional electrolytes [22, 23]. In contrast, optimizing the formation protocol strategy has garnered significant attention owing to its minimal additional production cost and its ability to precisely control the thermodynamics and kinetics of electrolyte decomposition evolving into the SEI [24–28].

The formation process, the initial charge–discharge cycle of LIBs before the real-world operation, involves the formation of inorganic components in the high-potential range (~3.0–1.5 V vs. Li^+/Li) and organic components in the low-potential range (~1.5–0.01 V vs. Li^+/Li) of graphite anodes (Figure 1a). $LiPF_6$, the predominant lithium salt used commercially, serves not only to conduct Li^+ but also decomposes to form LiF at potentials > 1.5 V [29]. Despite its inherent fluorine content from the PF_6^- anion, $LiPF_6$ is known for its poor film-forming ability and typically requires the introduction of various additives to form a robust and LiF-rich SEI, which increases LIBs' cost [30]. For example, the price of fluoroethylene carbonate (a widely used F additive in LIBs) is about 13 times that of $LiFP_6$. In this regard, constructing a LiF-rich SEI using $LiPF_6$ as the sole F source in the regular carbonate electrolyte demonstrates high industrialization value. While there are interesting studies on the film-forming regulation of the electrolyte in carbon anode [24, 27, 28], a strategy dedicated to establishing the chemical relationship between LiF-rich SEI and $LiPF_6$ has not been provided to date.

In this work, we discovered that $LiPF_6$ undergoes a decomposition pathway at ~2.28 V vs. Li^+/Li during formation at elevated temperatures (~80°C), generating abundant LiF nanoparticles at the graphite particle interface (Figure 1b). Consequently, we proposed a temperature-potential coupled formation (TPCF) strategy that integrates the thermodynamic properties of the electrolyte with electrochemical reactions. The TPCF protocol involves a constant-voltage charging step at ~2.28 V and 80°C to promote thorough decomposition of PF_6^-, thereby constructing a dense and LiF-rich inorganic inner layer. This is followed by a formation step at room temperature (25°C), allowing gradual reduction of solvent molecules to form a thin and uniform organic outer layer. The resulting SEI on graphite achieved via TPCF is thin, dense, and LiF grain boundary-rich, exhibiting lower energy barriers for Li^+ desolvation and diffusion through the SEI, along with a higher work function and Young's modulus. A graphite||$LiFePO_4$ pouch cell is used to evaluate the TPCF performance, demonstrating remarkable stability over 8940 cycles at 6C.

2 | Results and Discussion

2.1 | The Temperature-Potential Coupled Formation

The electrode potential for Li^+ intercalation into graphite is significantly lower than the electrochemical stability window of common electrolyte solvents and salts (>0.5 V vs. Li^+/Li), leading to irreversible reductive decomposition of the electrolyte and SEI formation [31, 32]. As a mixture of multiple components, the electrolyte's decomposition pathway during this process is influenced by both the potential and temperature conditions. Different temperatures can induce distinct thermodynamic decomposition pathways for various electrolyte components [24, 25, 33]. As shown in Figure 2a, cyclic voltammetry (CV) scans of the baseline electrolyte (1.1 M $LiPF_6$ in diethyl carbonate (DEC) and ethylene carbonate (EC) with 1:1 vol%) from the open-circuit potential (OCP) to 1.5 V vs. Li^+/Li across temperatures from 25°C to 100°C reveal a new reduction peak at ~2.28 V vs. Li^+/Li. In contrast, CV curves for a 1.1 M LiFSI baseline electrolyte under the same conditions show no obvious reduction peaks at either 25°C or 80°C (Figure 2b). This indicates that the electrochemical decomposition of $LiPF_6$ is highly temperature-dependent. Aside from $LiPF_6$ and LiFSI, the CV curves of LiDFOB at 25°C and 80°C (Figure S1) reveal that the temperature-potential-coupled decomposition behavior is governed by the chemical nature of the anion.

To exclude the influence of heating on the electrolyte solvent components, the 1.1 M $LiPF_6$ baseline electrolyte was subjected to 12 h of water bath heating, which produced no gas evolution, precipitation, or discoloration (Figure S2a,b). Furthermore, in situ variable-temperature ^{31}P nuclear magnetic resonance (NMR) (Figure S2c) and ^{19}F NMR (Figure S2d) spectra reveal no new peaks, except for those of PF_6^-. In situ variable-temperature Raman spectra show the high thermal stability of EC and DEC solvent molecules between 25°C–80°C (Figure S3), ruling out thermal decomposition of the solvents as a contributing factor. This confirms that PF_6^- does not undergo purely thermal decomposition between 25–80°C, and that its decomposition reaction at ~2.28 V requires the simultaneous satisfaction of both temperature and voltage conditions. Potentiostatic intermittent titration technique (PITT) results from graphite||lithium metal (Gr||Li) half cells at 25°C and 80°C further demonstrate that the reduction reaction occurs at 80°C within the potential range 2.45–2.12 V (Figure S4). The current peak corresponding to solvent reduction in the 1.5–0.01 V range is significantly stronger at 80°C than at 25°C, indicating that elevated temperature not only promotes salt decomposition but also intensifies solvent decomposition.

Based on the temperature-dependent electrochemical response of $LiPF_6$, a temperature-potential coupled formation (TPCF) protocol is established (Figure 2c): The graphite anode is first lithiated at 80°C with a constant current (CC mode) of 0.05C to 2.28 V, followed by a constant voltage (CV mode) hold at 2.28 V for 30 min, before finally being cooled to room temperature (25°C) and lithiated to 0.01 V at 0.1C. The constant-voltage step at 2.28 V fully utilizes anion decomposition. As shown in Figure 2d, the decomposition reaction essentially completes within 30 min, indicating that the graphite particle surfaces are fully covered

15213773, 2026, 10, Downloaded from https://onlinelibrary.wiley.com/doi/10.1002/anie.202525822 by Nanjing University Of Aeronautics And Astronautics, Wiley Online Library on [09/10/2026]. See the Terms and Conditions (https://onlinelibrary.wiley.com/terms-and-conditions) on Wiley Online Library for rules of use; OA articles are governed by the applicable Creative Commons License

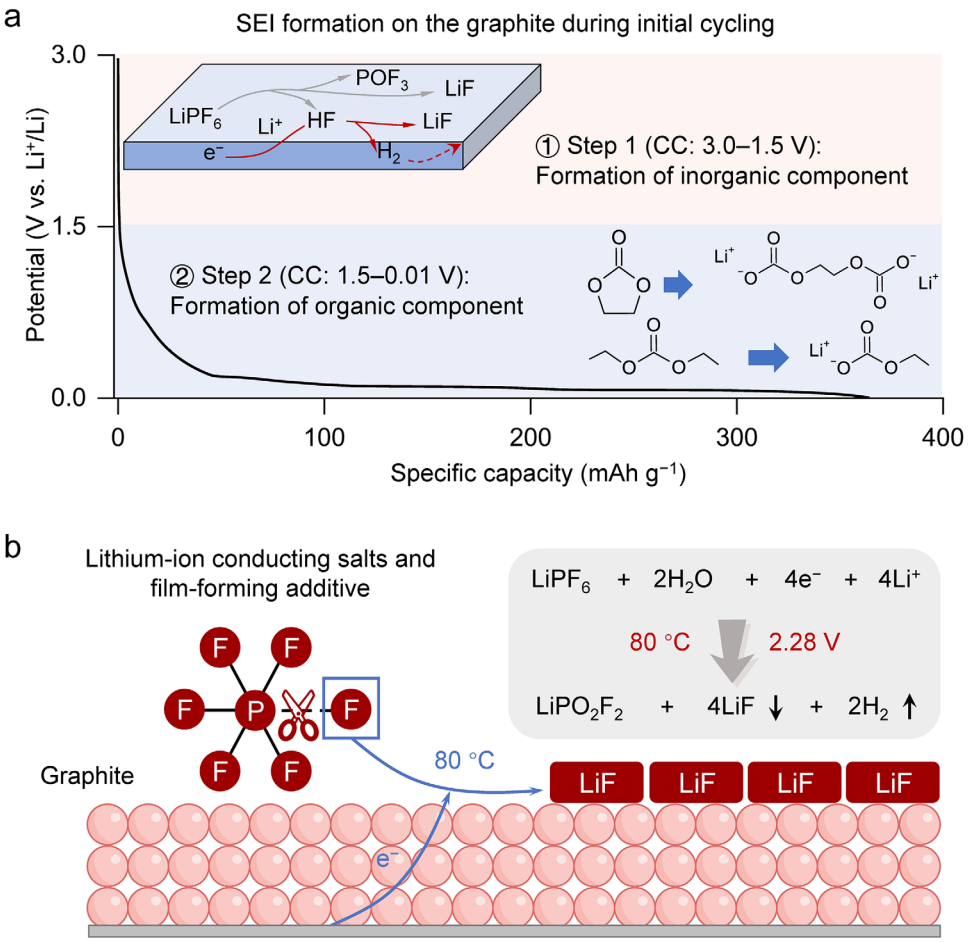


FIGURE 1 | (a) Electrochemical reaction processes involved in the formation of the SEI on graphite anodes during formation cycling. (b) Schematic illustration and reaction equation for LiF formation derived from PF_6^- decomposition at 80°C and ~2.28 V vs. Li^+/Li during formation.

with LiF, thereby blocking further electrolyte decomposition. Furthermore, the reduction peak intensities observed for electrolytes with varying $LiPF_6$ concentrations are nearly identical (Figure S5). Additionally, the theoretical minimum estimation of $LiPF_6$ consumption, as detailed in Note S1, indicates that a $LiPF_6$ concentration below 0.1 M is sufficient to fully cover the graphite particles and terminate the reaction. Galvanostatic charge–discharge (GCD) voltage profiles at different temperatures show that the formation step at 80°C does not adversely affect graphite lithiation/delithiation (Figure S6a). Differential capacity (dQ/dV) vs. voltage curves of 1.5–0.3 V (Figure S6b) also indicate that the extent of solvent reaction in TPCF is similar to room-temperature formation (RTF) and lower than in high-temperature formation (HTF) conducted entirely at 80°C. Consequently, the initial Coulombic efficiency (ICE) of TPCF is 94.0%, only 0.7% lower than RTF, whereas HTF exhibits a significantly lower ICE of 90.5% compared to 94.7% for RTF (Figure S6c).

Atomic force microscopy (AFM) was used to observe the morphology of the SEI formed on a highly oriented pyrolytic graphite (HOPG) electrode at different potentials and temperatures (Figures 2e–i) [34]. Compared to the inhomogeneous and sparse inorganic particles formed at 25°C and > 1.5 V, the electrode surface after the 80°C constant-voltage hold at 2.28 V is covered by a dense and uniform layer of inorganic particles. The nucleation of numerous inorganic particles is expected to form more grain boundaries, which are conducive to fast Li^+ transport. A thin organic layer covering inorganic particles is formed at 25°C and ~0.01 V, while a thicker organic layer is formed at 80°C and ~0.01 V. The pristine HOPG electrode surface is exceptionally flat (Figure S7a,b) with a height variation < 8 nm. In contrast, the HTF electrode interface exhibits the largest thickness fluctuation (Figure S8d,f), attributed to its thicker organic layer leading to SEI inhomogeneity. The TPCF electrode interface shows the smallest thickness variation (Figure S8c,e), indicating that a uniform and dense inorganic layer promotes homogeneous evolution of the organic layer. Thus, the TPCF protocol facilitates the formation of a stable, LiF-based SEI while suppressing excessive solvent decomposition, preventing the organic components of the SEI from becoming overly thick.

Nano-infrared (Nano-IR) spectroscopy coupled with AFM was used to detect the IR spectra of the respective electrodes (Figure 2j). The IR peaks corresponding to the C═O (1625 cm^{-1}) and C—O—C (1050 cm^{-1}) groups of lithium ethylene dicarbonate (LEDC) [35], a decomposition product of EC, are weak after formation at 25°C-1.5 V and 80°C-2.28 V, indicating minimal solvent decomposition in the high-potential range. Upon formation to 0.01 V, the HTF electrode surface shows the strongest signal, while the signal intensities for TPCF and RTF are similar. This confirms that HTF causes excessive decomposition of EC and

15213773, 2026, 10, Downloaded from https://onlinelibrary.wiley.com/doi/10.1002/anie.202525822 by Nanjing University Of Aeronautics And Astronautics, Wiley Online Library on [09/10/2026]. See the Terms and Conditions (https://onlinelibrary.wiley.com/terms-and-conditions) on Wiley Online Library for rules of use; OA articles are governed by the applicable Creative Commons License

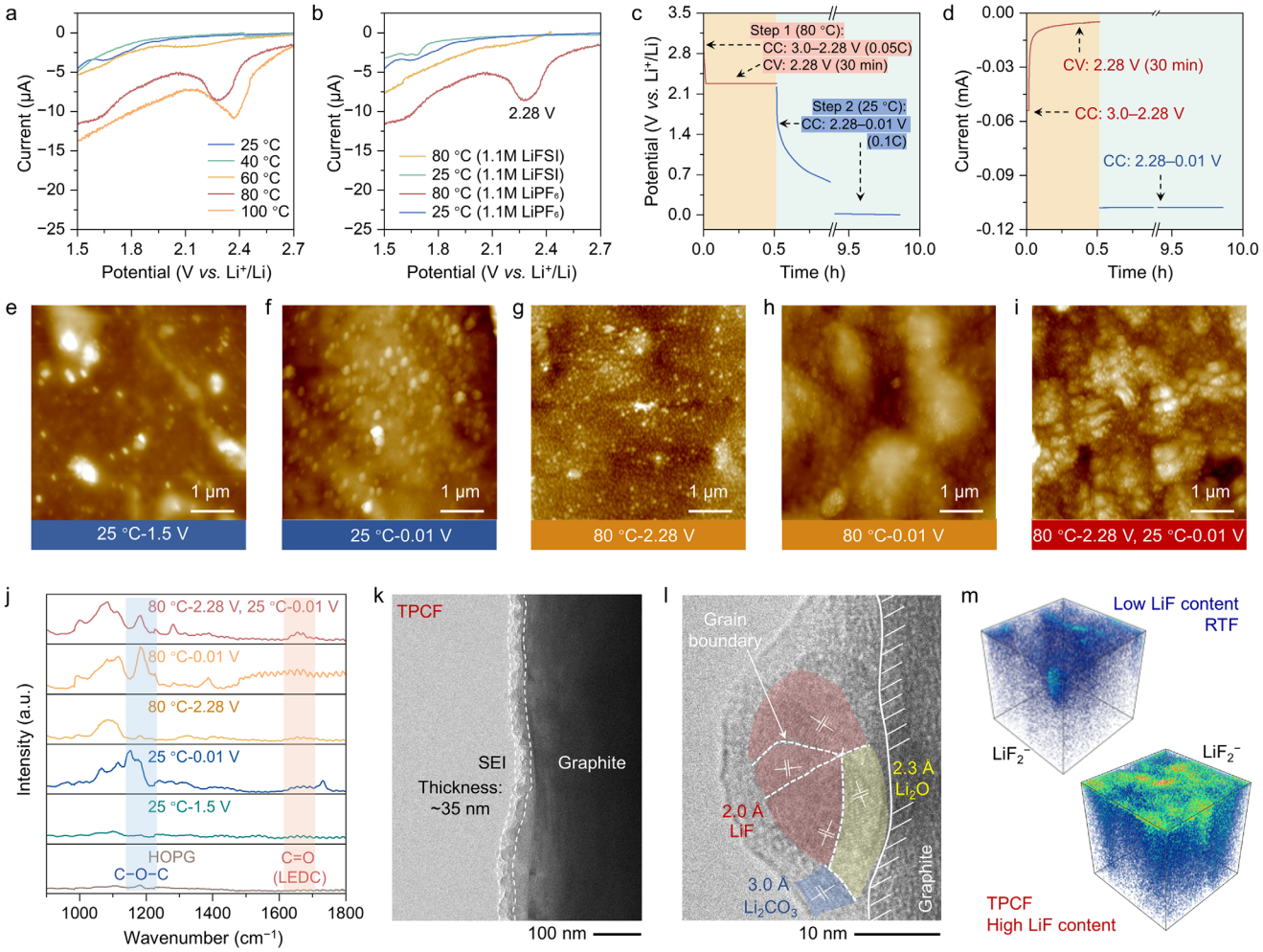


FIGURE 2 | (a) CV scans of the baseline electrolyte (1.1 M $LiPF_6$ in DEC and EC with 1:1 vol%) from the OCP to 1.5 V vs. Li^+/Li across a temperature range of 25°C to 100°C. (b) CV curves of 1.1 M $LiPF_6$ and 1.1 M LiFSI electrolytes measured at 25°C and 80°C. (c) Step configuration of the TPCF charging protocol and the corresponding charge voltage–time profile for a Gr||Li half cell. (d) Charge current–time profile corresponding to the TPCF protocol steps in panel (c). (e–i) AFM height images depicting the morphology of the SEI formed on a HOPG electrode after formation at different potentials under various temperatures. (j) Nano-IR spectra of the SEI on HOPG electrodes after formation under different temperature and potential conditions. (k, l) High-resolution cryo-TEM images of the SEI on graphite particles formed via the TPCF protocol. (m) Three-dimensional spatial distribution of LiF_2^- fragments derived from TOF-SIMS characterization of the SEI on graphite particles subjected to RTF and TPCF protocols.

DEC solvent molecules, generating large amounts of organic compounds like LEDC and lithium alkyl carbonates (e.g., LEC) in the SEI's outer layer. The coverage by a relatively thin organic layer in TPCF and RTF can block further reduction reactions, preventing the formation of an excessively thick SEI film. Two-dimensional IR imaging at 1625 cm^{-1} (Figure S9) further shows that the TPCF electrode is uniformly covered by organics, whereas the RTF electrode exhibits uneven organic coverage.

High-resolution cryogenic transmission electron microscopy (cryo-TEM) images of the SEI on graphite particles formed via TPCF (Figure 2k,l and Figure S10c) reveal a thin SEI layer with a thickness of only ~18–35 nm, which is lower than that of RTF (Figure S10a,b). The inner SEI layer in TPCF primarily consists of LiF inorganic particles, covered by an amorphous organic layer embedded with Li_2CO_3 microcrystals. The inner LiF is not a single crystal but rather a polycrystalline aggregate with multiple orientations. The grain boundaries between microcrystalline regions are expected to facilitate fast Li^+ transport [10]. The LiF originates from the decomposition of PF_6^-, while the outer Li_2CO_3 likely results from further evolution of LEDC [36]. To validate the large-scale consistency of the SEI, complementary low-magnification scanning electron microscopy (SEM) and energy-dispersive x-ray spectroscopy (EDS) characterizations were performed (Figure S11). It demonstrated that the SEI formed via TPCF exhibits superior morphological homogeneity compared to that formed via RTF. Furthermore, quantitative EDS analysis confirmed a higher F content and a lower O content on the TPCF anode, providing macroscale evidence that TPCF facilitates the formation of a LiF-rich SEI. Time-of-flight secondary ion mass spectrometry (TOF-SIMS) characterization of the SEI on graphite particles via RTF and TPCF, providing three-dimensional spatial distribution information for LiF_2^-, CHO_2^-, and $PO_2F_2^-$ fragments (Figure 2m and Figure S12), indicates that the SEI of TPCF contains more LiF and $LiPO_2F_2$ inorganic products, while the CHO_2^- fragment, representing lithium alkyl carbonates (organic components), is less abundant compared to RTF.

15213773, 2026, 10, Downloaded from https://onlinelibrary.wiley.com/doi/10.1002/anie.202525822 by Nanjing University Of Aeronautics And Astronautics, Wiley Online Library on [09/10/2026]. See the Terms and Conditions (https://onlinelibrary.wiley.com/terms-and-conditions) on Wiley Online Library for rules of use; OA articles are governed by the applicable Creative Commons License

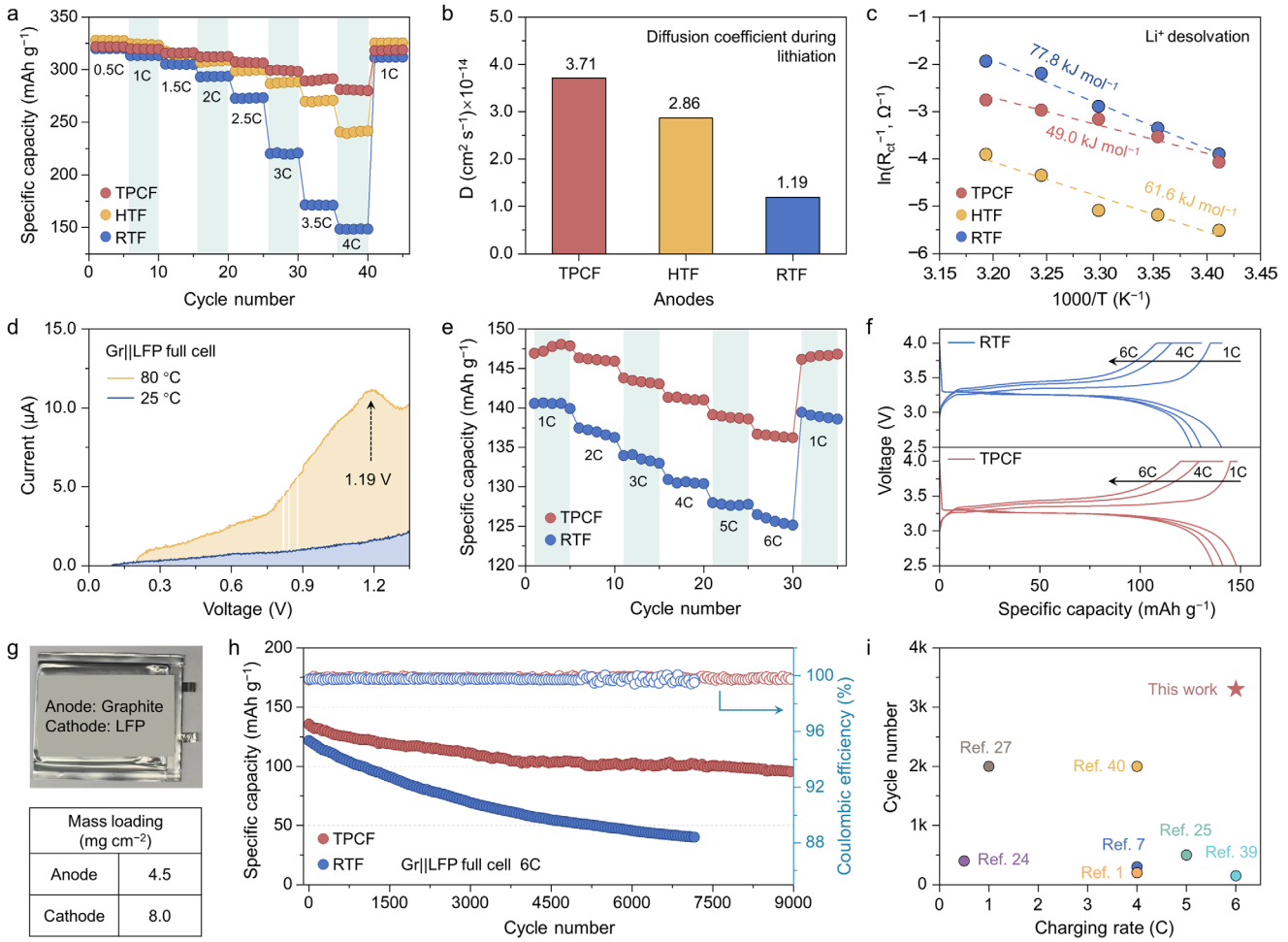


FIGURE 3 | (a) Rate performance of TPCF, HTF, and RTF Gr||Li half cells within the voltage range of 0.01–2.0 V. (b) Li^+ diffusion coefficients during the lithiation process for TPCF, HTF, and RTF graphite electrodes, determined from variable-scan-rate CV. (c) The $E_{a,ct}$ values for TPCF, HTF, and RTF anodes, obtained from variable-temperature EIS. (d) CV curves of Gr||LFP full cells measured at 80°C and 25°C with a scan rate of 0.1 mV s^{-1}. (e) Rate capability of TPCF and RTF pouch cells. (f) GCD voltage profiles (under CC–CV mode) for TPCF and RTF pouch cells at 1C, 4C, and 6C rates. (g) Digital photograph and electrode mass loading of Gr||LFP pouch cells. (h) Long-term cycling performance of TPCF and RTF pouch cells at 6C. (i) Comparison of fast-charging performance with previously reported electrolyte engineering strategies.

2.2 | Fast-Charging Performance

The interfacial modification effects of different formation protocols were evaluated using Gr||Li half cells. As shown in Figure 3a, the specific capacities of TPCF, HTF, and RTF Gr||Li half cells cycled at a low rate of 0.5C are comparable, ranging between 320–330 mAh g^{-1}. However, when the rate increases to 2.5C, the RTF graphite electrode begins to exhibit performance degradation. At 4C, TPCF remains stable with a specific capacity of ~280 mAh g^{-1}, while both HTF and RTF show significant degradation, with specific capacities of ~241 and 148 mAh g^{-1}, respectively. The corresponding charge–discharge profiles of TPCF, HTF, and RTF at various rates from 1C–4C are presented in Figure S13a. The results indicate that the severe degradation of HTF and RTF at high rates primarily occurs within the 0.06–0.01 V voltage plateau. Potential relaxation profiles after discharging at 0.2C show that the TPCF anode reaches a steady state faster than HTF and RTF, suggesting faster Li^+ transport across the TPCF graphite particle interface and consequently lower polarization (Figure S13b). The TPCF electrode maintains stability over 200 cycles at a high rate of 4C (Figure S13c), with a capacity retention of 99.1%, significantly higher than RTF (83.0%) and HTF (92.4%). As shown in Figure 3b and Figure S14, the Li^+ diffusion coefficients during lithiation, calculated from variable-scan-rate CV [34], confirm that the higher specific capacity retention of the TPCF anode at high rates originates from its higher Li^+ diffusion rate. Furthermore, the diffusion rates within the electrodes, calculated from electrochemical impedance spectroscopy (EIS) (Figure S15) [37], are consistent with the variable-scan-rate CV results. In contrast, comparing the bulk diffusion rates within the graphite particles measured by the galvanostatic intermittent titration technique (PITT) (Figure S16) reveals that the formation protocol modification did not alter the intrinsic bulk diffusion properties of graphite. Therefore, the improved diffusion rate in the TPCF electrode is attributed to the enhanced SEI interface. By reducing interfacial diffusion resistance, the deposition of Li plating at high rates is suppressed, thereby enabling stable fast charging and long-term cycling.

To deconvolute the mechanism of interfacial modification on Li^+ transport enhancement, the activation energies for Li^+ desolvation and its transport across the SEI were calculated

15213773, 2026, 10, Downloaded from https://onlinelibrary.wiley.com/doi/10.1002/anie.202525822 by Nanjing University Of Aeronautics And Astronautics, Wiley Online Library on [09/10/2026]. See the Terms and Conditions (https://onlinelibrary.wiley.com/terms-and-conditions) on Wiley Online Library for rules of use; OA articles are governed by the applicable Creative Commons License

from variable-temperature EIS based on the Arrhenius equation (Figures 3c and S17) [16]. The results show that the TPCF graphite interface exhibits the lowest charge transfer activation energy ($E_{a,ct}$) of 49.0 kJ mol^{-1}, while the $E_{a,ct}$ for HTF graphite (61.6 kJ mol^{-1}) is also considerably lower than that of RTF (77.8 kJ mol^{-1}). This is attributed to the dense LiF-rich inorganic layer within the SEI, which facilitates rapid desolvation of Li^+ from its solvation shell. Additionally, the activation energy for Li^+ transport across the SEI ($E_{a,SEI}$) for HTF is higher than that for TPCF and RTF, due to the increased thickness of the organic layer in HTF's SEI, resulting in a longer transport distance for Li^+. Figure S18 schematically illustrates the transport of solvated Li^+ across the graphite electrode interfaces for RTF, HTF, and TPCF. The sparse inorganic particles in the SEI via RTF lead to incomplete desolvation of solvated Li^+ as they migrate through the organic layer toward the graphite surface, increasing the difficulty of electron transfer to Li^+. Although HTF exhibits enhanced desolvation capability and faster Li^+ diffusion via grain boundaries due to its denser inorganic layer, the overall resistance for solvated Li^+ crossing the SEI is increased by its thicker organic layer. In contrast, TPCF achieves a densified inorganic layer while effectively controlling the organic-layer thickness, resulting in lower overall resistance for solvated Li^+ across the SEI, coupled with stronger desolvation capability and faster transport of bare Li^+ through grain boundaries. Ultimately, this reduces the total impedance from both SEI transport and charge transfer, enabling fast charging.

To validate the practical applicability of TPCF, full cells composed of graphite anodes and $LiFePO_4$ (LFP) cathodes were tested. First, as shown in Figure S19, a three-electrode cell (Gr|Li Ref.|LFP) incorporating a lithium metal reference electrode (Li Ref.) was assembled to determine the full-cell charging voltage corresponding to the graphite potential of 2.28 V vs. Li^+/Li. For the formation at 80°C and 0.1 C, the corresponding Gr||LFP full-cell voltage is 1.19 V when the Gr|Li Ref. potential reaches 2.28 V. Consequently, the TPCF constant voltage step for the full cell at 80°C was set at 1.19 V, followed by formation to 4 V at 25°C. CV curves of the full cell (Figure 3d) also show a new reduction peak at 1.19 V only during the 80°C formation, consistent with the three-electrode cell results. A broad reduction peak is observed when charging to 4 V at 80°C (Figure S20), indicating severe side reactions of the electrolyte at the high oxidation potential of the cathode. GCD voltage profiles at 0.1C of full cells (Figure S21a) show that HTF exhibits significantly reduced discharge capacity and lower ICE (72.7%) in Figure S21b. Thus, formation over the entire voltage range at 80°C is detrimental to full cells. TPCF prevents damage to the cell electrolyte caused by high temperatures and high oxidation potentials, achieving a CE of 86.7%, which is slightly lower than that of RTF (88.4%). This difference is consistent with the results obtained from the Gr||Li half cells, indicating that the LFP cathode contributes only minimally to electrolyte oxidation in the low-potential range under high-temperature conditions.

As shown in Figure 3e, under the CC–CV mode charging protocol, the TPCF pouch cell outperforms RTF across rates from 1C–6C. The corresponding charge–discharge voltage profiles at 1C, 4C, and 6C rates (Figure 3f) indicate that the poor rate capability of RTF is due to larger polarization during fast charging. Hybrid pulse power characterization (HPPC) tests further confirm the higher ohmic polarization of the RTF electrode (Figure S22) [28]. This suggests that the dense inorganic layer of the SEI via TPCF, containing abundant grain boundaries, facilitates faster Li^+ transport, thereby reducing polarization. Notably, as shown in Figure 3g,h, the TPCF electrode demonstrates exceptional stability during long-term cycling at a high 6C rate, exceeding 8940 cycles with a capacity retention of 70.5% (3304 cycles to reach 80% capacity retention). In contrast, the RTF electrode's capacity dropped to 54.2% after 3300 cycles and to 33.0% after 7157 cycles. This is attributed to the smaller charge transfer resistance of the TPCF electrode (Figure S23). The significantly increased impedance of the RTF electrode after long-term cycling is likely due to substantial Li plating caused by high-rate polarization, leading to accumulated dead Li at the interface. Correspondingly, SEM images after long-term cycling confirmed that the pores of the RTF electrode are blocked by dead Li, while the TPCF anode retained a well-preserved porous structure (Figure S24).

Chronoamperometry (CA) tests show a lower leakage current for the TPCF electrode (Figure S25). This is ascribed to the TPCF-derived SEI, resulting in less consumption of active Li^+ due to repeated SEI growth/dissolution during 6C long-term cycling. The contact potential difference (CPD) measured by Kelvin probe force microscopy (KPFM) [38] for TPCF and RTF electrodes (Figure S26) yields a calculated work function of 7.57 eV for TPCF, substantially higher than the 4.85 eV for RTF. This further indicates the superior electronic insulation of the TPCF-derived SEI. On the other hand, the SEI at the TPCF graphite interface exhibits a Young's modulus (Figure S27) that is two to three times higher (~6–9 GPa) than that of RTF (~2–4 GPa). Consequently, it can suppress Li dendrite formation more effectively during fast charging, thereby contributing to improved electrode cycling stability. As shown in Figure 3i, the fast-charging rate and cycling stability of the TPCF electrode compare favorably with the fast-charging performance reported in other electrolyte engineering studies [1, 7, 24, 25, 27, 39, 40].

2.3 | The Mechanism of Temperature-Potential Coupling

To elucidate the temperature-potential coupled reaction mechanism for the conversion of $LiPF_6$ to LiF, characterization of the resulting triphasic products was conducted. First, in situ ^{31}P and ^{19}F NMR was used to detect liquid products dissolved in the electrolyte after formation at 25°C and 80°C to different potentials (Figure 4a,b). The results indicate a distinct $PO_2F_2^-$ peak in the electrolyte after formation at 80°C-2.28 V, whereas no significant changes were observed after formation at 25°C-1.5 V (Figure S28). Gaseous products generated during TPCF and RTF were analyzed by differential electrochemical mass spectrometry (DEMS), comparing the yields of H_2 evolved at 80°C-2.28 V and 25°C-1.5 V (Figure 4c and Figure S29a) and C_2H_4 evolved at 80°C and 25°C-0.01 V (Figure S29b,c). TPCF produced significantly more H_2 than RTF, while yielding slightly less C_2H_4. This suggests that PF_6^- undergoes more intense hydrolysis in the high-potential region, generating LiF alongside substantial H_2 as a byproduct. In the low-potential region, where TPCF proceeds at the same temperature as RTF, the dense inorganic inner layer reduces the decomposition of solvents like EC, resulting in less C_2H_4 formation.

15213773, 2026, 10, Downloaded from https://onlinelibrary.wiley.com/doi/10.1002/anie.202525822 by Nanjing University Of Aeronautics And Astronautics, Wiley Online Library on [09/10/2026]. See the Terms and Conditions (https://onlinelibrary.wiley.com/terms-and-conditions) on Wiley Online Library for rules of use; OA articles are governed by the applicable Creative Commons License

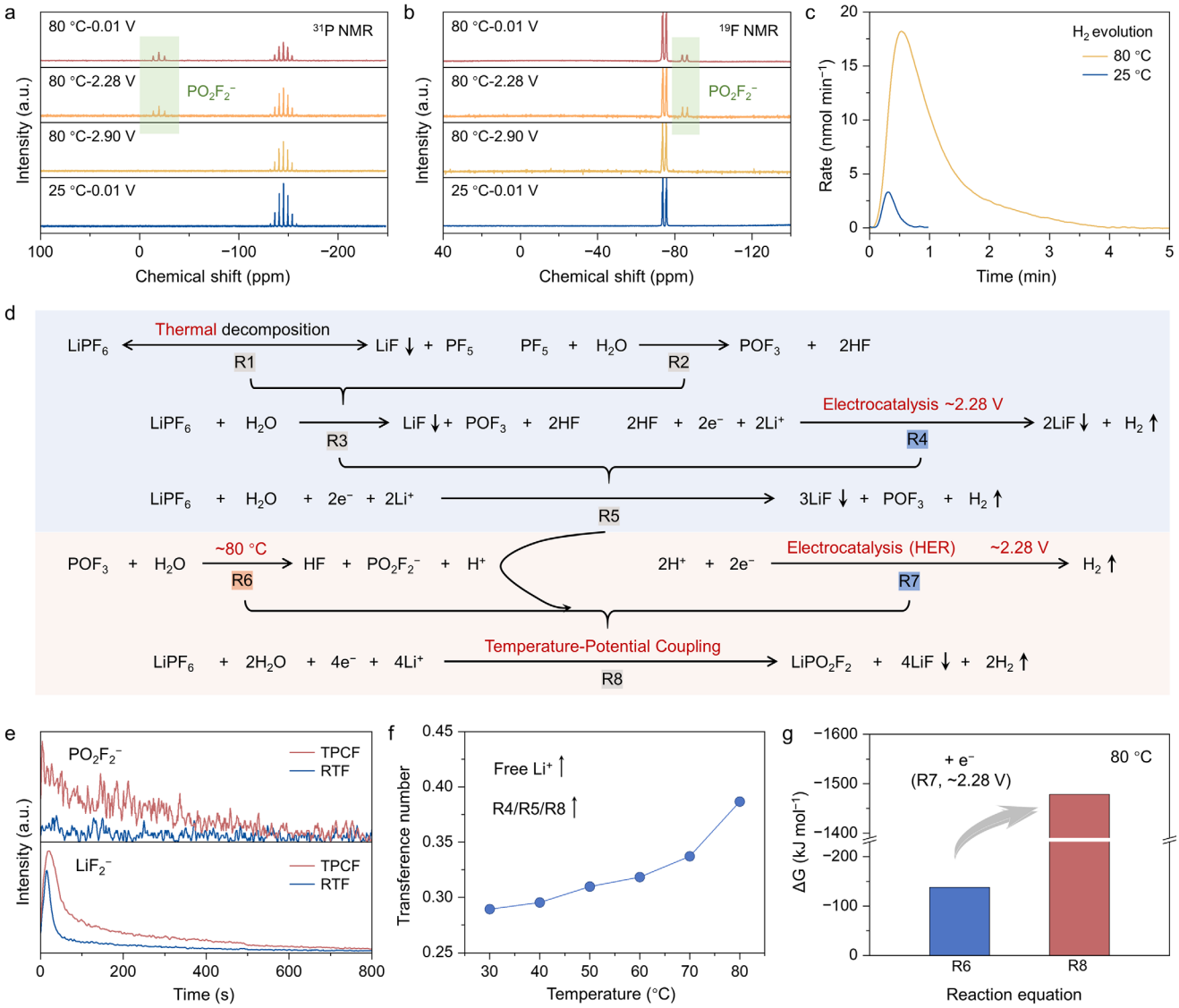


FIGURE 4 | (a, b) In situ ^{31}P and ^{19}F NMR spectra of liquid products in the electrolyte during formation at 25°C and 80°C to different potentials. (c) Quantification of H_2 gas evolution detected by DEMS during formation at 25°C-1.5 V and 80°C-2.28 V. (d) Proposed chemical reaction pathway for the evolution of $LiPF_6$ to LiF at 80°C and 2.28 V during formation. (e) Depth profiles showing the abundance of LiF_2^- and $PO_2F_2^-$ fragments obtained by TOF-SIMS sputtering. (f) Li^+ transference number of the employed electrolyte in the temperature range of 30–80°C. (g) Variation in the Gibbs free energy for reaction equations R6 and R8 from 25°C to 80°C.

Integrating the aforesaid results, the triphasic products generated during the SEI formation at 80°C-2.28 V are identified as: 1) solid LiF deposited on graphite particles, 2) liquid $PO_2F_2^-$ dissolved in the electrolyte, and 3) gaseous H_2 evolved. This leads to the proposed chemical reaction pathway for $LiPF_6$ evolving into LiF at 80°C and 2.28 V, as depicted in Figure 4d. Typically, $LiPF_6$ first undergoes reversible thermal decomposition to LiF and PF_5 (R1), with PF_5 subsequently reacting with H_2O (R2) [29]. However, in situ heating characterization of the electrolyte indicates that thermal energy alone drives weak $LiPF_6$ decomposition. The electrochemical reaction (R4), which catalyzes the conversion of the product HF to LiF and H_2, is crucial for promoting the continuous occurrence of R3. Therefore, the overall process constitutes a coupled thermal-electrochemical reaction (R5).

At the elevated temperature of 80°C, a new decomposition pathway (R6) emerges: POF_3 further hydrolyzes, producing HF, $PO_2F_2^-$, and H^+. Based on calculations in Note S2 and CV results, H^+ undergoes the hydrogen evolution reaction (HER) at ~2.28 V (R7) [41]. Thus, the elevated temperature intensifies hydrolysis in R6, while the electrocatalytic HER at 2.28 V continuously consumes the H^+ produced in R6, shifting the equilibrium of R6 to the right and promoting the reaction continuously, ultimately yielding abundant LiF (R8). The consistent trends in the abundance of LiF_2^- and $PO_2F_2^-$ ion fragments with increasing TOF-SIMS sputtering depth (Figure 4e) provide indirect evidence for the occurrence of R8. The Li^+ transference number of the electrolyte increases with temperature (Figure 4f), indicating that elevated temperature also liberates more Li^+ to facilitate LiF formation reactions (R4/R5/R8) within the SEI. In situ variable-

15213773, 2026, 10, Downloaded from https://onlinelibrary.wiley.com/doi/10.1002/anie.202525822 by Nanjing University Of Aeronautics And Astronautics, Wiley Online Library on [09/10/2026]. See the Terms and Conditions (https://onlinelibrary.wiley.com/terms-and-conditions) on Wiley Online Library for rules of use; OA articles are governed by the applicable Creative Commons License

temperature Raman spectroscopy further confirms a decrease in Li^+ solvation degree (Figure S30) [42, 43]. Calculations of the Gibbs free energy for R6 and R8 confirm that the potential-driven HER (R7) promotes the occurrence of R8 (Figure 4g).

Overall, the temperature-potential coupled mechanism is as follows: Temperature governs the occurrence of R6, while the potential controls R4 (providing the POF_3 reactant for R6) and simultaneously drives R7 (continuously consuming the H^+ product from R6). Hence, their synergy promotes R8, leading to the complete coverage of graphite particle surfaces with LiF, which subsequently blocks the R8 reaction.

3 | Conclusion

In this work, we proposed an industrially viable TPCF strategy that leverages the electrochemical decomposition of $LiPF_6$ at 2.28 V-80 °C to construct a thin and LiF-rich solid-electrolyte interphase (SEI) on graphite anodes. The TPCF protocol not only overcomes the inherent limitations of $LiPF_6$ as a poor SEI-forming agent but also eliminates the need for expensive fluorinated additives, offering a cost-effective and scalable approach to enhance fast-charging performance in commercial lithium-ion batteries. A coupled thermal-electrochemical reaction mechanism that promotes the complete decomposition of PF_6^- into LiF was unveiled, while effectively controlling the thickness and composition of the SEI. The resulting SEI exhibits lower energy barriers for Li^+ desolvation and transport, as well as superior electronic insulation, as evidenced by its higher work function and Young's modulus. These properties collectively suppress Li plating and dendrite formation, enabling exceptional cycling stability even under extreme fast-charging conditions. The TPCF protocol demonstrated remarkable practicality by integrating seamlessly into existing battery manufacturing processes without introducing additional materials or complex procedures. The graphite||$LiFePO_4$ full cell achieves over 8940 cycles at a 6C rate (full charge in 10 min) with 70.5% capacity retention. An 80% capacity retention was achieved after 3304 cycles, with this fast-charging performance and cycling stability surpassing those reported in other state-of-the-art electrolyte engineering studies. This performance, coupled with the use of commercially dominant $LiPF_6$ and conventional carbonate electrolytes, positions TPCF as a highly transferable and economically feasible technology for next-generation fast-charging batteries in electric vehicles and beyond. This work provides both fundamental insights into the thermodynamics and kinetics of electrolyte decomposition and a practical pathway toward the industrial realization of high-performance, long-lasting fast-charging lithium-ion batteries.

Acknowledgments

This work was financially supported by the National Key R&D Program of China (2021YFB2400300), the National Natural Science Foundation of China (52573335), the Natural Science Foundation of Shanghai (25ZR1401207), the CATL Future Energy Research Institute (22H010102023), and the Fundamental Research Funds for the Central Universities (25X010202131). Z. Liang acknowledges Shanghai TANSUO Testing and Inspection Company for the assistance on AFM, SEM, and TEM characterizations.

Conflicts of Interest

The authors declare no conflict of interest.

Data Availability Statement

The data that support the findings of this study are available from the corresponding author upon reasonable request.

References

1. C.-X. Zhao, Z. Wang, D. Jacobson, et al., "Electrolytes That Reduce Electro-Osmotic Drag Improve Fast Charging of Lithium-Ion Batteries," *Science* 390 (2025): 745–750, https://doi.org/10.1126/science.adv1739.

2. Y. Dong, C. Liu, M. Rui, et al., "Review on Graphite Anodes for Fast-Charging Lithium-Ion Batteries: Mechanism, Modification and Characterizations," *Advanced Functional Materials* 35 (2025): 2506190, https://doi.org/10.1002/adfm.202506190.

3. H. Liu, L. Zhao, Y. Ye, et al., "Extremely Fast-Charging Batteries: Principle, Strategies, Detection, and Prediction," *Chemical Reviews* 125 (2025): 9553–9678, https://doi.org/10.1021/acs.chemrev.5c00203.

4. R. He, W. Zhong, Y. Wu, et al., "Two-Layer Graphite Anode for Energy and Power Densified $LiFePO_4$ Battery," *Advanced Materials* 37 (2025): 2501185, https://doi.org/10.1002/adma.202501185.

5. W. Cai, Y.-X. Yao, G.-L. Zhu, et al., "A Review on Energy Chemistry of Fast-Charging Anodes," *Chemical Society Reviews* 49 (2020): 3806–3833, https://doi.org/10.1039/C9CS00728H.

6. S.-Y. Sun, X.-Q. Zhang, Y.-N. Wang, J.-L. Li, Z. Zheng, and J.-Q. Huang, "Understanding the Transport Mechanism of Lithium Ions in Solid-Electrolyte Interphase in Lithium Metal Batteries With Liquid Electrolytes," *Materials Today* 77 (2024): 39–65, https://doi.org/10.1016/j.mattod.2024.06.001.

7. C. Song, S. H. Han, Y. Choi, et al., "Geometric Design of Interface Structures and Electrolyte Solvation Chemistry for Fast Charging Lithium-Ion Batteries," *Advanced Materials* 37 (2025): 2418773, https://doi.org/10.1002/adma.202418773.

8. Y.-H. Tan, Z. Liu, J.-H. Zheng, et al., "Inorganic Composition Modulation of Solid Electrolyte Interphase for Fast Charging Lithium Metal Batteries," *Advanced Materials* 36 (2024): 2404815, https://doi.org/10.1002/adma.202404815.

9. S. Chen, Z. Deng, J. Li, et al., "Tuning Reaction Kinetics of Fluorinated Molecules to Construct Robust Solid Electrolyte Interphases on SiO_x Anode," *Angewandte Chemie International Edition* 64, (2025): e202413927.

10. S. Wu, Y. Zhang, H. Liang, et al., "In-Situ Electrochemical Customization of Solid Electrolyte Interphase for Fast-Charging and Long-Cycle-Life Graphite Anodes," *Energy Storage Mater* 75 (2025): 104024, https://doi.org/10.1016/j.ensm.2025.104024.

11. H. Xie, L. Liu, H. Chen, et al., "Fast-Charging Phosphorus Anodes Enabled by Fluorinated Weakly Solvated Electrolytes for Stable and High-Rate Lithium Storage," *Advanced Materials* 37 (2025): 2504248, https://doi.org/10.1002/adma.202504248.

12. G. Zhang, T. Zhang, Z. Zhang, et al., "High-Energy and Fast-Charging Lithium Metal Batteries Enabled by Tuning Li^+-Solvation via Electron-Withdrawing and Lithiophobicity Functionality," *Nature Communications* 16 (2025): 4722, https://doi.org/10.1038/s41467-025-59967-w.

13. J. Xu, J. Zhang, T. P. Pollard, et al., "Electrolyte Design for Li-Ion Batteries Under Extreme Operating Conditions," *Nature* 614 (2023): 694–700, https://doi.org/10.1038/s41586-022-05627-8.

14. Y. Ou, W. Hou, D. Zhu, et al., "Molecular Design of Electrolyte Additives for High-Voltage Fast-Charging Lithium Metal Batteries," *Energy & Environmental Science* 18 (2025): 1464–1476, https://doi.org/10.1039/D4EE04282D.

15. W. Zhang, Y. Lu, Q. Feng, et al., "Multifunctional Electrolyte Additive for High Power Lithium Metal Batteries at Ultra-Low Temperatures,"

15213773, 2026, 10, Downloaded from https://onlinelibrary.wiley.com/doi/10.1002/anie.202525822 by Nanjing University Of Aeronautics And Astronautics, Wiley Online Library on [09/10/2026]. See the Terms and Conditions (https://onlinelibrary.wiley.com/terms-and-conditions) on Wiley Online Library for rules of use; OA articles are governed by the applicable Creative Commons License

Nature Communications 16 (2025): 3344, https://doi.org/10.1038/s41467-025-58627-3.

16. S. Tu, B. Zhang, Y. Zhang, et al., "Fast-Charging Capability of Graphite-Based Lithium-Ion Batteries Enabled by Li_3P-Based Crystalline Solid–Electrolyte Interphase," *Nature Energy* 8 (2023): 1365–1374, https://doi.org/10.1038/s41560-023-01387-5.

17. C. Wang, Y. Xie, Y. Huang, et al., "Li3 PO 4-Enriched SEI on Graphite Anode Boosts Li^+ De-Solvation Enabling Fast-Charging and Low-Temperature Lithium-Ion Batteries," *Angewandte Chemie International Edition* 63 (2024): e202402301, https://doi.org/10.1002/anie.202402301.

18. M. Niu, L. Dong, J. Yue, et al., "A Fast-Charge Graphite Anode With a Li-Ion-Conductive, Electron/Solvent-Repelling Interface," *Angewandte Chemie International Edition* 63 (2024): e202318663, https://doi.org/10.1002/anie.202318663.

19. S. Lee, H. Lee, H. Chang, et al., "Ester-Guided Dynamic Li^+ Solvation Enables Plating-Less, Fast-Charging Li-Ion Batteries," *ACS Nano* 19 (2025): 15789–15802, https://doi.org/10.1021/acsnano.5c00027.

20. Y. Wang, Y. Ji, Z.-W. Yin, et al., "Tuning Rate-Limiting Factors for Graphite Anodes in Fast-Charging Li-Ion Batteries," *Advanced Functional Materials* 34 (2024): 2401515, https://doi.org/10.1002/adfm.202401515.

21. D. J. Kautz, X. Cao, P. Gao, et al., "Designing Electrolytes With Controlled Solvation Structure for Fast-Charging Lithium-Ion Batteries," *Advanced Energy Materials* 13 (2023): 2301199, https://doi.org/10.1002/aenm.202301199.

22. C. Song, S. H. Han, H. Moon, and N.-S. Choi, "Unlocking Fast-Charging Capabilities of Lithium-Ion Batteries Through Liquid Electrolyte Engineering," *EcoMat* 6 (2024): e12476.

23. S. Kang, G. Ma, Y. Liu, et al., "Progress in Fast-Charging Graphite Anodes for Lithium-Ion Batteries: Reaction Kinetics," *Energy Storage Mater* 81 (2025): 104531, https://doi.org/10.1016/j.ensm.2025.104531.

24. R. Hou, L. Zheng, T. Shi, et al., "An Unexpected Low-Temperature Battery Formation Technology Enabling Fast-Charging Graphite Anodes," *Advanced Functional Materials* 35 (2025): 2500481, https://doi.org/10.1002/adfm.202500481.

25. L. Hong, Y. Zhang, P. Mei, et al., "Temperature-Responsive Formation Cycling Enabling LiF-Rich Cathode-Electrolyte Interphase," *Angewandte Chemie International Edition* 63 (2024): e202409069.

26. H. Wang, Y. Liu, M. Jiang, et al., "The Potential Regulation of Working Anode for Long-Term Zero-Volt Storage at 37°C in Li-Ion Batteries," *Advanced Materials* 36 (2024): 2400656, https://doi.org/10.1002/adma.202400656.

27. C. Zhong, J. Zhu, X. Li, et al., "Rapidly-Formed Interphase Facilitating Fast-Charging Lithium-Ion Batteries," *ACS Energy Letters* 10 (2025): 4627–4635, https://doi.org/10.1021/acsenergylett.5c02398.

28. Y. J. Ha, S. Roh, B. K. Park, et al., "Innovative Fast-Charging Protocol Incorporating Proactive Lithium-Plating Suppression Pulses for Lithium-Ion Batteries: Protocol Design, Validation, and Post-Mortem Analysis," *Advanced Energy Materials* 14 (2024): 2402032, https://doi.org/10.1002/aenm.202402032.

29. T. Liu, L. Lin, X. Bi, et al., "In Situ Quantification of Interphasial Chemistry in Li-Ion Battery," *Nature Nanotechnology* 14 (2019): 50–56, https://doi.org/10.1038/s41565-018-0284-y.

30. F. Zhang, Z. Wang, L. Wang, et al., "Constructing a Universal Artificial Polymeric Ionic Liquid Interfacial Film for Graphite Anode and High-Voltage Cathode," *Chemical Engineering Journal* 435 (2022): 135101, https://doi.org/10.1016/j.cej.2022.135101.

31. E. Peled, "The Electrochemical Behavior of Alkali and Alkaline Earth Metals in Nonaqueous Battery Systems—The Solid Electrolyte Interphase Model," *Journal of the Electrochemical Society* 126 (1979): 2047–2051, https://doi.org/10.1149/1.2128859.

32. K. Xu, "Nonaqueous Liquid Electrolytes for Lithium-Based Rechargeable Batteries," *Chemical Reviews* 104 (2004): 4303–4418, https://doi.org/10.1021/cr030203g.

33. Y. Qian, Q. Dong, R. Yi, et al., "Heated-to-Frozen Electrochemical Interphase Formation Strategy Enables Stable 4.5 V Li-Metal Batteries in Ether-Based Electrolyte," *ACS Energy Letters* 10 (2025): 3962–3971, https://doi.org/10.1021/acsenergylett.5c01200.

34. S. Li, Y. Zhang, S. Wu, et al., "Synchronized Achieving Amount Reduction and Efficiency Increase of Lithium Salt-Type Additive by Alternating Current Pulse Discharge Technology," *Chemical Engineering Journal* 485 (2024): 150095, https://doi.org/10.1016/j.cej.2024.150095.

35. A. Dopilka, Y. Gu, J. M. Larson, V. Zorba, and R. Kostecki, "Nano-FTIR Spectroscopy of the Solid Electrolyte Interphase Layer on a Thin-Film Silicon Li-Ion Anode," *ACS Applied Materials & Interfaces* 15 (2023): 6755–6767, https://doi.org/10.1021/acsami.2c19484.

36. S. K. Heiskanen, J. Kim, and B. L. Lucht, "Generation and Evolution of the Solid Electrolyte Interphase of Lithium-Ion Batteries," *Joule* 3 (2019): 2322–2333, https://doi.org/10.1016/j.joule.2019.08.018.

37. T. Q. Nguyen and C. Breitkopf, "Determination of Diffusion Coefficients Using Impedance Spectroscopy Data," *Journal of the Electrochemical Society* 165 (2018): E826–E831, https://doi.org/10.1149/2.1151814jes.

38. L. Dong, H.-J. Yan, Q.-X. Liu, et al., "Quantification of Charge Transport and Mass Deprivation in Solid Electrolyte Interphase for Kinetically-Stable Low-Temperature Lithium-Ion Batteries," *Angewandte Chemie International Edition* 63 (2024): e202411029.

39. X. Yue, J. Zhang, Y. Dong, et al., "Reversible Li Plating on Graphite Anodes Through Electrolyte Engineering for Fast-Charging Batteries," *Angewandte Chemie International Edition* 62 (2023): e202302285, https://doi.org/10.1002/anie.202302285.

40. C.-Y. Wang, T. Liu, X.-G. Yang, et al., "Fast Charging of Energy-Dense Lithium-Ion Batteries," *Nature* 611 (2022): 485–490, https://doi.org/10.1038/s41586-022-05281-0.

41. X. Yuan, M. T. Bender, M. Ko, and K.-S. Choi, "Understanding Two Voltammetric Features of Water Reduction and Water Oxidation in Mild pH Solutions," *Nature Catalysis* 8 (2025): 495–506, https://doi.org/10.1038/s41929-025-01339-0.

42. T. Zheng, T. Xu, J. Xiong, et al., "Multipoint Anionic Bridge: Asymmetric Solvation Structure Improves the Stability of Lithium-Ion Batteries," *Advancement of Science* 11 (2024): 2410329, https://doi.org/10.1002/advs.202410329.

43. J. Yin, X. Zhu, Y. Zhang, et al., "Vinyl Silane-Mediated Solvation Energetics Enable High-Voltage Lithium-Ion Batteries," *Advanced Energy Materials* 15 (2025): e04022, https://doi.org/10.1002/aenm.202504022.

Supporting Information

Additional supporting information can be found online in the Supporting Information section.

Supporting File 1: anie71314-sup-0001-SuppMat.docx.

15213773, 2026, 10, Downloaded from https://onlinelibrary.wiley.com/doi/10.1002/anie.202525822 by Nanjing University Of Aeronautics And Astronautics, Wiley Online Library on [09/10/2026]. See the Terms and Conditions (https://onlinelibrary.wiley.com/terms-and-conditions) on Wiley Online Library for rules of use; OA articles are governed by the applicable Creative Commons License